

Article

Self-Separation of a Single Ultrashort Light Pulse in the Parametric Raman Anti-Stokes Laser Based on a CaMoO₄ Crystal under Intracavity Synchronous Pumping

Dmitry P. Tereshchenko ¹, Sergei N. Smetanin ^{1,2,*} , Alexander G. Papashvili ¹, Yury A. Kochukov ^{1,2}, Anatoly I. Titov ¹, Evgeny V. Shashkov ¹, Maria D. Lapina ², Vladislav E. Shukshin ¹, Kirill A. Subbotin ¹ , and Denis A. Lis ¹

¹ Research Center for Laser Materials and Technologies, Prokhorov General Physics Institute of the Russian Academy of Sciences, Vavilova 38, 119991 Moscow, Russia; tereshchenko.mitya2018@yandex.ru (D.P.T.)

² College of New Materials and Nanotechnologies, National University of Science and Technology MISiS, Leninski Prospekt 4, 119049 Moscow, Russia

* Correspondence: ssmetanin@bk.ru

Abstract: The effect of the self-separation of a single ultrashort light pulse of a parametric Raman CaMoO₄ laser with birefringence phase matching under intracavity synchronous pumping by a mode-locked 1064 nm Nd:YAG laser is experimentally investigated and theoretically simulated. The conditions for the self-separation effect for the single ultrashort pulse at an anti-Stokes wavelength of 973 nm with the pulse duration of 9 ps and the pulse energy of up to 9 μJ are defined.

Keywords: Raman crystal; parametric Raman interaction; synchronous pumping; ultrashort pulse



Citation: Tereshchenko, D.P.;

Smetanin, S.N.; Papashvili, A.G.;

Kochukov, Y.A.; Titov, A.I.; Shashkov,

E.V.; Lapina, M.D.; Shukshin, V.E.;

Subbotin, K.A.; Lis, D.A.

Self-Separation of a Single Ultrashort Light Pulse in the Parametric Raman Anti-Stokes Laser Based on a CaMoO₄ Crystal under Intracavity Synchronous Pumping. *Crystals* **2023**, *13*, 636. <https://doi.org/10.3390/cryst13040636>

Academic Editor: Francesco Simoni

Received: 23 March 2023

Revised: 5 April 2023

Accepted: 5 April 2023

Published: 7 April 2023



Copyright: © 2023 by the authors. Licensee MDPI, Basel, Switzerland. This article is an open access article distributed under the terms and conditions of the Creative Commons Attribution (CC BY) license (<https://creativecommons.org/licenses/by/4.0/>).

1. Introduction

The use of resonant nonlinearity of stimulated Raman scattering (SRS) makes it possible to carry out intracavity parametric Raman four-wave interactions that allow controlling the spectral-temporal structure of laser radiation, if a phase-matching condition is fulfilled for this [1–3]. Intracavity control by laser radiation characteristics is an emerging field, including an intracavity mode convertor [4] and intracavity spatiotemporal metasurfaces [5]. Using the intracavity pumping for Raman lasers with the phase-matched parametric coupling of SRS radiation components allowed the achievement of strong self-shortening for the oscillated SRS pulses as well as the self-separation of a single ultrashort pulse of the anti-Stokes radiation [6,7].

The main cause for the wave mismatch of the parametric four-wave mixing of SRS components is the refractive index dispersion of a Raman-active medium. Using the laser wavelength close to a zero dispersion wavelength of the active crystal [7] or fiber [8] allowed the achievement of four-wave interactions with SRS simultaneously. The implementation of a non-collinear four-wave interaction at arbitrary laser wavelengths [2,3] allowed the solving of the wave mismatch problem; however, the efficiency of anti-Stokes oscillation in the studied crystals turned out to be very low, which can be explained by the narrow angular tolerance of phase matching at the non-collinear interaction [9].

Birefringent crystals are widely used in the nonlinear optics of media with quadratic nonlinearity to fulfill phase-matching conditions for collinear orthogonally polarized three-wave interactions [10]. The maintenance of similar birefringence phase-matching conditions for collinear orthogonally polarized four-wave interactions on the SRS nonlinearity was first implemented for CaCO₃ in [11]. This was later applied to coherent anti-Stokes Raman spectroscopy in [12–14], and also for the efficient parametric Raman anti-Stokes lasers [9,15]. The collinear interaction was organized due to tangential phase matching insensitive to angular mismatch compensating the walk-off effect for extraordinary waves relative to the

ordinary waves under the interaction in the highly birefringent CaCO_3 crystal. Recently, a parametric Raman anti-Stokes laser was experimentally achieved using collinear phase matching insensitive to angular mismatch due to the choice of a SrWO_4 Raman-active crystal with optimal birefringence when pumping by a Nd:YAG laser oscillating at a 532 nm second harmonic generation [16].

In the present work, the conditions of the self-separation of a single ultrashort anti-Stokes pulse from the output radiation pulse train in the parametric Raman anti-Stokes CaMoO_4 laser with the collinear phase matching insensitive to angular mismatch under intracavity synchronous pumping by a mode-locked 1064 nm Nd:YAG laser are experimentally investigated and theoretically simulated. For the first time, to our knowledge, a high-quality self-separation of a single ultrashort anti-Stokes pulse is achieved in a passively mode-locked parametric Raman laser.

2. Raman Crystal Characterization

A CaMoO_4 crystal crystallizes in the tetragonal scheelite-type structure of C_{4h}^6 space symmetry. The approximation of almost free anions $(\text{MoO}_4)^{2-}$ can be applied to this compound because covalent bonds between Mo and four oxygen atoms are stronger than a bond between the full $(\text{MoO}_4)^{2-}$ tetragonal anionic group with the Ca^{2+} cation sublattice. Internal vibrations corresponding to the oscillations inside the $(\text{MoO}_4)^{2-}$ anionic groups with an immovable mass center create the narrowest and most intense lines in a Raman scattering spectrum and can be used for SRS. CaMoO_4 , as with other related scheelite-type tetragonal crystals, is a promising active medium for Raman lasers [17]. The intensity of the main vibrational mode (symmetric stretching vibration of $(\text{MoO}_4)^{2-}$ with a wave number $\nu_R = 879 \text{ cm}^{-1}$) of the CaMoO_4 crystal is only 1.5 times lower than for the “closest relative”—the SrMoO_4 crystal, which has proven itself as an efficient SRS converter [18–20]. However, the implementation of SRS in CaMoO_4 was carried out only in two works [21,22]. In [21], the possibility of the multifunctional operation of the Nd:CaMoO₄ crystal was also shown as an active medium of a self-Raman laser. The attractive side of the CaMoO_4 crystal is also its manufacturability—it can be grown using cheap and environmentally friendly materials, as well as inexpensive and well-developed melt technologies, in particular, by the Czochralski technique in air [23].

Another remarkable property of scheelite-type crystals is the presence of birefringence characterized by a difference in the main values of the refractive index $|n_e - n_o|$, which provides the possibility of fulfilling the collinear phase-matching condition for four-wave interactions on the resonant nonlinearity of Raman scattering [16,24,25]. The problem for this is a narrow angular tolerance of phase matching and a walk-off effect [16,25]. As shown in [16], the solution to the problem can be the use of crystals with a large phase-matching angle in the range of 60° – 90° , observed in the optimal birefringence range of the crystal $|n_e - n_o| = 0.005$ – 0.015 (analyzed for a number of Raman-active crystals when pumped with a wavelength of $\lambda_p = 532 \text{ nm}$), which provides a phase-matching insensitive to angular mismatch for four-wave-mixing anti-Stokes generation at a wavelength $\lambda_{aS} = (2\lambda_p^{-1} - \lambda_S^{-1})^{-1}$, where $\lambda_S = (\lambda_p^{-1} - \nu_R)^{-1}$ is a wavelength of the Stokes SRS radiation.

The expressions for calculation of the phase-matching angle Θ_{pm} and the angular tolerance $\Delta\Theta_{pm}$ of phase matching for Stokes–anti-Stokes parametric Raman coupling were determined in [16] for the *ooee* (*eeoo*) type of phase matching in a positive (negative) uniaxial crystal. It means that, in a positive crystal (*ooee* type), the extraordinary probe wave at λ_p is scattered into the extraordinary anti-Stokes wave at λ_{aS} due to the parametric process if the active medium is coherently driven by the SRS process when the ordinary probe wave at λ_p is scattered into the ordinary Stokes wave at λ_S .

Figure 1 demonstrates an overview diagram of the phase-matching characteristics (Θ_{pm} and $\Delta\Theta_{pm}$) of parametric Raman anti-Stokes generation under pumping at $\lambda_p = 1064 \text{ nm}$ calculated from these expressions for several uniaxial Raman-active crystals depending on their birefringence $|n_e - n_o|$. The refractive index data for CaCO_3 ($\nu_R = 1086 \text{ cm}^{-1}$,

$|n_e - n_o| = 0.163$), LiIO_3 ($\nu_R = 770 \text{ cm}^{-1}$, $|n_e - n_o| = 0.14$), PbMoO_4 ($\nu_R = 870 \text{ cm}^{-1}$, $|n_e - n_o| = 0.10$), CaWO_4 ($\nu_R = 911 \text{ cm}^{-1}$, $|n_e - n_o| = 0.015$), and CaMoO_4 ($\nu_R = 879 \text{ cm}^{-1}$, $|n_e - n_o| = 0.0066$) were taken from [26].

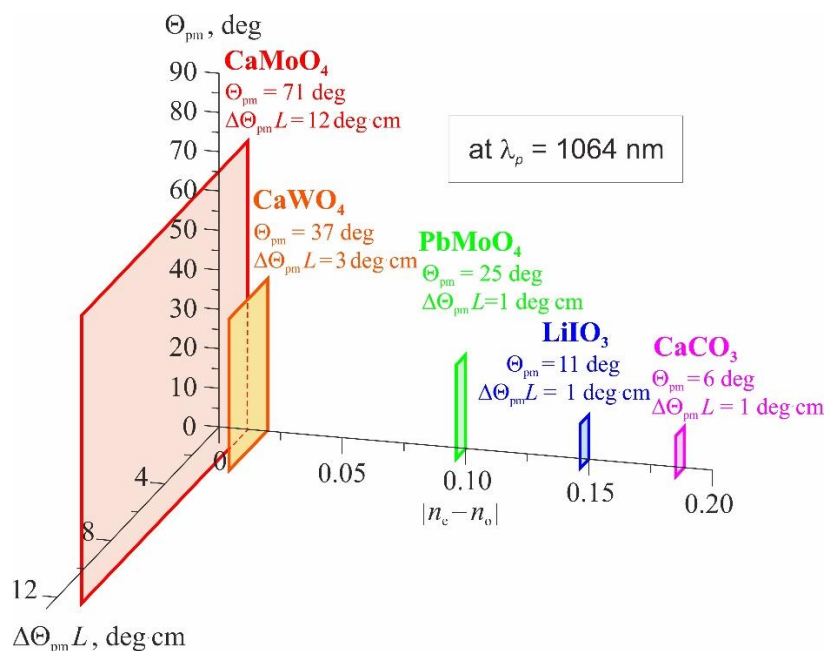


Figure 1. Overview diagram of the phase-matching characteristics (Θ_{pm} and $\Delta\Theta_{pm}$) of parametric Raman anti-Stokes generation under pumping at $\lambda_p = 1064 \text{ nm}$ for known uniaxial Raman-active crystals depending on their birefringence.

It can be seen from Figure 1 that the crystals with a high birefringence of $|n_e - n_o| > 0.05$ have a low phase-matching angle of $\Theta_{pm} < 25^\circ$ and a narrow angular tolerance of $\Delta\Theta_{pm} < 1^\circ/L$, where L is the crystal length (in cm). Decreasing the crystal birefringence to lower than $|n_e - n_o| < 0.015$ results in increasing the phase-matching angle to $\Theta_{pm} > 37^\circ$ and widening the angular tolerance to $\Delta\Theta_{pm} > 3^\circ/L$.

Among the described crystals, the CaMoO_4 crystal with the lowest birefringence of $|n_e - n_o| = 0.0066$ has the widest angular tolerance ($\Delta\Theta_{pm} = 12^\circ/L$) because the phase-matching angle of $\Theta_{pm} = 71^\circ$ is quite close to noncritical 90° -phase matching, which is insensitive to angular mismatch.

We can also check crystals with lower birefringence, for example, SrMoO_4 ($\nu_R = 888 \text{ cm}^{-1}$, $|n_e - n_o| = 0.0028$) [26]. However, the phase-matching condition at $\lambda_p = 1064 \text{ nm}$ cannot be fulfilled for this crystal because of its birefringence is too low.

The angular tolerance problem is also connected with a walk-off problem expressed by the walk-off angle of $\beta = \Theta_{pm} - \arctan(n_e^2/n_o^2 \cdot \tan\Theta_{pm})$ limiting an effective length of the interaction [10]. A walk-off of the spot of an extraordinary wave from the spot of an ordinary wave at the crystal output face amounts to $L \cdot \tan\beta$. At the CaMoO_4 crystal length of $L = 3 \text{ cm}$, we obtain a very small walk-off of $L \cdot \tan\beta \approx 0.06 \text{ mm}$ ($\beta \approx 2 \text{ mrad}$). In comparison, for CaWO_4 and PbMoO_4 at $L = 3 \text{ cm}$, we have an essentially higher walk-off of $L \cdot \tan\beta \approx 0.22 \text{ mm}$ ($\beta \approx 7.5 \text{ mrad}$) and $L \cdot \tan\beta \approx 1.02 \text{ mm}$ ($\beta \approx 34 \text{ mrad}$), respectively. It should be noted that the pump radiation usually needs to be focused into an active crystal to implement SRS, so the walk-off problem is acute: the walk-off ($L \cdot \tan\beta$) should be significantly less than the focused beam radius.

For the research, an active element was prepared from a CaMoO_4 crystal with a length of 30 mm, cut in the phase-matching direction ($\Theta_{pm} = 71^\circ$), with plane-parallel polished faces. The crystal was grown by us by the Czochralski technique in an air atmosphere at the "Kristall-2" installation from a platinum–rhodium crucible with a diameter of 40 mm and a height of 40 mm using a charge prepared from CaCO_3 and MoO_3 reagents of the ACS qualification. A single-crystal seed was oriented perpendicularly to the optical (main

crystallographic) axis, the pulling speed was 3 mm/h, and the rotation speed was 6 rpm. After the growth was completed and the crystal was detached from the melt mirror, it was slowly cooled to 300 K at a speed of 8 K/h in order to avoid cracking. The necessary orientation of the crystal in the above phase-matching direction was performed on the Biomed-5 polarization microscope with crossed polarizers in direct transmitted light.

Figure 2 shows the measurement results of polarized Raman spectra for the prepared CaMoO₄ crystal oriented at the phase-matching angle of $\Theta_{pm} = 71^\circ$. The sample was excited by continuous-wave laser radiation with a wavelength of 532 nm and an average power of 70 mW. The radiation scattered by the sample was collected according to a 180° scheme (“back-scattering”) and decomposed into a spectrum using a double monochromator “SPEX-Ramalog 1403”. The hardware resolution and sampling of the spectrum during registration were 1 cm⁻¹.

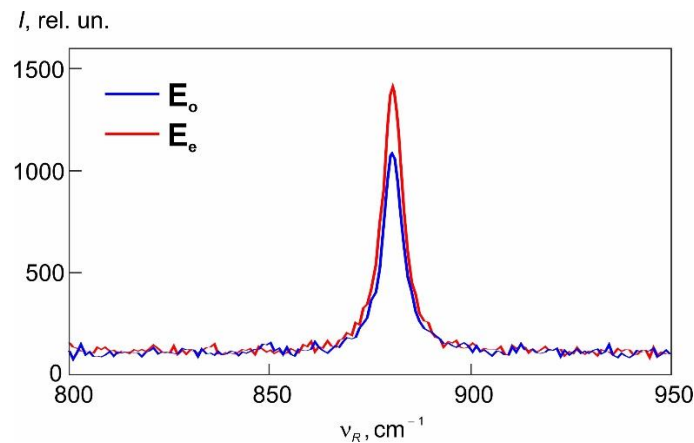


Figure 2. Polarized spontaneous Raman scattering spectra of the CaMoO₄ crystal cut at the phase matching angle of $\Theta_{pm} = 71^\circ$ for excitation by ordinary (E_o) and extraordinary (E_e) light waves.

As can be seen from Figure 2, the ratio of the intensity of the most intense stretching A_g line (at $\nu_R = 879 \text{ cm}^{-1}$) of the vibrational spectrum when interacting with ordinary waves to its intensity when interacting with extraordinary waves is $I_o/I_e = 0.77$. With a similar measurement for a CaMoO₄ crystal oriented in the perpendicular direction to the optical axis, this ratio is $I_o/I_e = 0.73$. Consequently, when oriented at the phase-matching angle (71°), the I_e value decreased slightly—by about 5%—compared to the orientation in the main direction (90°). At the pump wavelength of $\lambda_p = 1064 \text{ nm}$, the Raman gain coefficient of the CaMoO₄ crystal when pumped by an extraordinary wave polarized along the crystal optical axis is $g_e = 4.3 \text{ cm/GW}$ [22], whereas when pumped by an ordinary wave, it amounts to $g_o = 3.1 \text{ cm/GW}$ (the Raman gain coefficient is proportional to the intensity of the vibrational line, so $g_o/g_e = 0.73$). The A_g line width is $\Delta\nu_R = 5.5 \text{ cm}^{-1}$.

In a CaMoO₄ crystal with tetragonal symmetry, the Raman scattering tensor for the stretching A_g line has the following form [27]:

$$\left(\frac{\partial\alpha}{\partial Q}\right)_{A_g} = \begin{pmatrix} a & 0 & 0 \\ 0 & a & 0 \\ 0 & 0 & b \end{pmatrix}, \quad (1)$$

where the a and b components of the tensor are proportional to the square root of the g_o and g_e Raman gain coefficients, respectively. We can determine a parametric coupling coefficient for four-wave mixing of orthogonally polarized waves. For the ooe type of phase matching, the parametric coupling coefficient p is proportional to $a^2\cos^2\Theta + absin^2\Theta$ [14]; therefore, in the phase-matching direction, it can be defined as

$$p = g_o\cos^2\Theta_{pm} + \sqrt{g_o g_e}\sin^2\Theta_{pm}, \quad (2)$$

Then, its value is equal to $p = 3.6 \text{ cm/GW}$ (at $g_o = 3.1 \text{ cm/GW}$, $g_e = 4.3 \text{ cm/GW}$ and $\Theta_{pm} = 71^\circ$).

3. Laser System

The optical scheme of the laser system is presented in Figure 3.

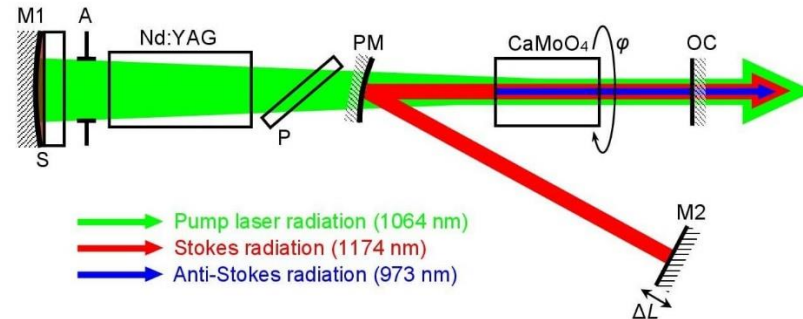


Figure 3. Optical scheme of the laser system: Nd:YAG and CaMoO₄ are the active elements of the pump laser and the parametric Raman laser, respectively; M1 and M2 are the end mirrors of the pump laser and the parametric Raman laser, respectively; S is the passive laser shutter (dye) at the M1 mirror; PM is the pumping mirror of the parametric Raman laser; OC is the output coupler of the laser system; A is the aperture; and P is the thin-film polarizer.

A lamp-pumped Nd:YAG rod with a diameter of 6.3 mm and a length of 100 mm was used as an active element of the pump laser. An aperture A with a diameter of 2 mm was used to select a fundamental TEM₀₀ transversal mode in the pump laser. A passive laser shutter S carried out a hybrid regime of passive Q-switching and mode locking of the pump laser cavity. A circulating layer (about 300 μm thick) of a dye No. 3274 solution [28] in acetonitrile was used as the passive laser shutter, which was in optical contact with a highly reflective mirror M1 (reflection coefficient of 99.1% at the pump laser wavelength of $\lambda_p = 1064 \text{ nm}$). The pump laser had a semispherical cavity, i.e., the cavity length was close to the radius of curvature ($\rho_{M1} = 1400 \text{ mm}$) of the concave end mirror M1. Firstly, it contributed to stable mode locking of the pump laser cavity due to the fact that the semispherical cavity is located at the stability diagram edge. Secondly, such cavity configuration provided a decrease in the radius of the pump laser beam in the active CaMoO₄ element by r_1/r_2 times (r_1 and r_2 are the radii of the pump laser radiation beam in the active Nd:YAG and CaMoO₄ elements, respectively) to intensify the intracavity pumping of the parametric Raman laser. The thin-film polarizer P provided a linear (horizontal) polarization of the pump laser radiation.

The above-described CaMoO₄ crystal with a length of 30 mm, cut at the phase-matching angle of $\Theta_{pm} = 71^\circ$, was used as the active element of the parametric Raman laser. The length of the V-shaped cavity of the parametric Raman laser was aligned with the length of the pump laser cavity by means of a longitudinal displacement (ΔL) of an end mirror M2 (reflection coefficient of 99.7% at the Stokes radiation wavelength of $\lambda_s = 1174 \text{ nm}$) mounted on a precision translation stage, which provided the intracavity synchronous pumping of SRS in the parametric Raman laser.

All mirrors of the laser system had reflection coefficients below 20% at an anti-Stokes radiation wavelength of $\lambda_{as} = 973 \text{ nm}$; therefore, the anti-Stokes radiation was generated parametrically in a single pass through the CaMoO₄ element. The pumping mirror PM was concave ($\rho_{PM} = 1000 \text{ mm}$) to ensure the alignment of the radii of the beams of the Stokes SRS radiation and the pump laser radiation in the active CaMoO₄ element. The PM mirror was highly reflective for the Stokes radiation (reflection coefficient of 99.6%), but transmitting for the pump laser radiation (transmission coefficient of 97.5%; an anti-reflection coating was applied to the non-working face of the PM mirror). The output coupler OC was flat and had reflection coefficients of $R_{973} = 12\%$, $R_{1064} = 96\%$, and $R_{1173} = 86\%$ at the wavelengths of the anti-Stokes ($\lambda_{as} = 973 \text{ nm}$), pump laser ($\lambda_p = 1064 \text{ nm}$), and Stokes ($\lambda_s = 1174 \text{ nm}$) radiation, respectively.

The active CaMoO_4 element was installed on a precision rotation stage with the axis of rotation coinciding with the axis of the laser beam. This made it possible to rotate the active CaMoO_4 element by an angle φ relative to the horizontal plane, increasing the relative proportion of the ordinary wave in the pump laser radiation (at $\varphi = 0$, the optical axis of the CaMoO_4 crystal lay in the horizontal plane; then, the horizontally polarized radiation of the pump laser was an extraordinary wave). The function of this rotation was to optimize the *ooee*-type parametric four-wave mixing.

The geometry of the optical elements arrangement in the laser system was chosen according to the calculations of the intracavity beams of the pump and Stokes radiation using the ReZonator software (<http://rezonator.orion-project.org>, accessed on 11 July 2022). According to the optimized calculation results, the optical length of both cavities (the pump laser and the parametric Raman laser) was chosen to be 1350 mm (near the stability diagram edge of the pump laser cavity), and the active CaMoO_4 element was located in the position of equal beam radii ($\approx 600 \mu\text{m}$) of the pump laser and Stokes radiations. In this case, the ratio of the radii of the pump laser beam in the active Nd:YAG and CaMoO_4 elements was $r_1/r_2 \approx 1.5$.

4. Experimental Study

The use of an intracavity aperture made it possible to obtain the oscillation of the fundamental transversal TEM_{00} mode. The separate registration of various frequency components of laser radiation was provided by using a diffraction grating at the laser output, which decomposed the output laser radiation into a spectrum.

The initial transmittance of the passive laser shutter of the pump laser was chosen to be low, 40%, by changing the dye concentration in the solution to overcome SRS threshold in the parametric Raman laser. The pulse energy of lamp pumping was set to be equal to 34 J, which corresponded to near-threshold oscillation of the pump laser at $\lambda_p = 1064 \text{ nm}$ in a stable mode-locking regime with a train of ultrashort radiation pulses having a duration of the bell-shaped envelope of 90 ns (at half-width) with the ultrashort pulse repetition period in the pulse train equal to 9 ns (9 ultrashort pulses in the pulse train).

SRS conversion into the Stokes radiation ($\lambda_s = 1174 \text{ nm}$) in the parametric Raman laser was obtained at the synchronization of pumping by detuning the parametric Raman laser cavity length, ΔL . The sensitivity of the synchronously-pumped SRS to the ΔL detuning had a scale of 10 mm. Blocking the M2 mirror (Figure 3) led to stopping SRS, which confirms the participation of the parametric Raman laser cavity in SRS conversion. The adjustment of the rotation angle (φ) of the active CaMoO_4 element also provided parametric Raman conversion into the anti-Stokes radiation.

Figure 4 shows the spectra of three output radiation components decomposed by a diffraction grating after frequency doubling by a lithium iodate crystal. Frequency doubling was used to visualize the output radiation components: the pump laser radiation was green (532 nm), the Stokes radiation was yellow (587 nm), and the anti-Stokes radiation was blue (486.5 nm). It also made it possible to use a spectrometer for visible radiation, OceanOpticsHR2000 (200–1000 nm), which has a high resolution (0.4 nm). However, the width of the spectral lines of the generated radiation components did not exceed the resolution of the spectrometer. The spectral line of anti-Stokes radiation was recorded not only in the second harmonic generation (486.5 nm), but also directly in the fundamental harmonic generation (973 nm). Figure 4 also demonstrates that the anti-Stokes beam spot has a beam profile close to Gaussian with a high beam quality.

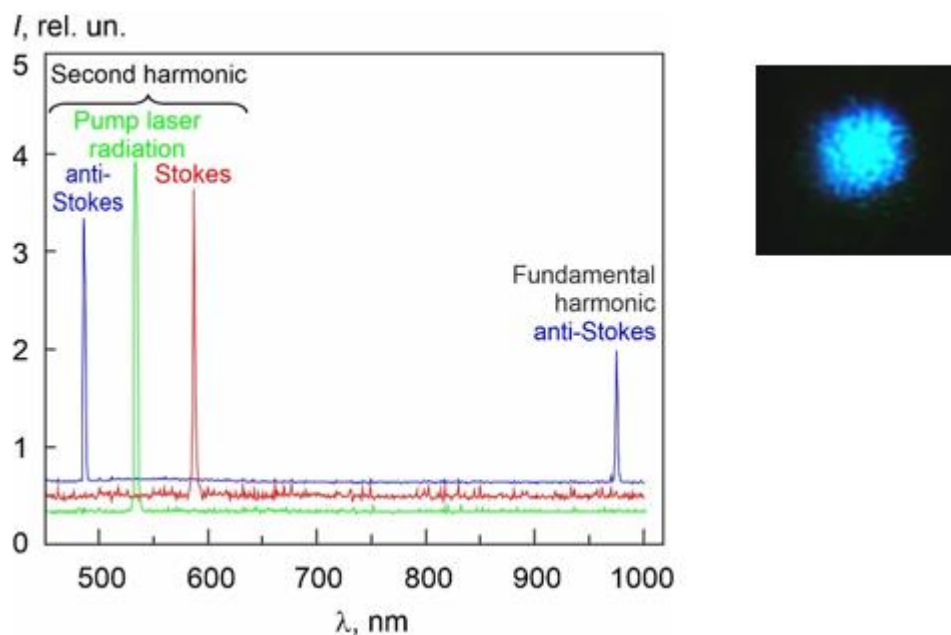


Figure 4. Spectra of the three output radiation components decomposed by a diffraction grating after frequency doubling and a photo of the anti-Stokes second-harmonic beam spot.

Figure 5 shows the oscillograms of the laser radiation at the rotation angle of the active CaMoO₄ element equal to $\varphi = 27^\circ$ (Figure 5a) and $\varphi = 32^\circ$ (Figure 5b). The oscillograms for all three components of the output radiation (separated by a diffraction grating) were recorded simultaneously using three avalanche photodiodes LFD-2A connected to a four-channel oscilloscope, LeCroy WaveSurfer 3054 (500 MHz).

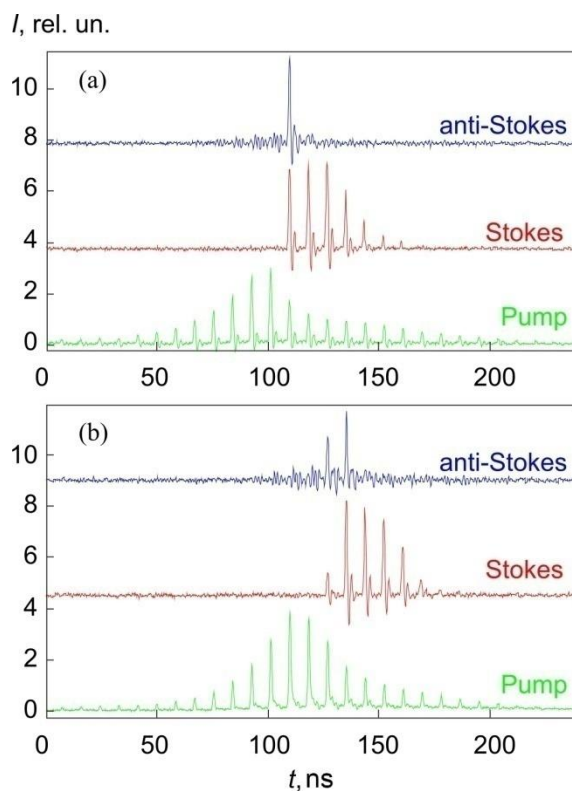


Figure 5. Oscillograms of the laser radiation at the rotation angle of the active CaMoO₄ element equal to (a) $\varphi = 27^\circ$ and (b) $\varphi = 32^\circ$.

It can be seen from Figure 5a that the value of $\varphi = 27^\circ$ provided a high-quality self-separation of the single ultrashort anti-Stokes pulse from the output radiation pulse train. A similar pattern of the generation of a single anti-Stokes pulse was also obtained at $\varphi < 27^\circ$, but with a lower anti-Stokes pulse energy. At $\varphi > 27^\circ$, the quality of the self-separation of a single anti-Stokes pulse was sharply reduced. Figure 5b demonstrates such a situation at $\varphi = 32^\circ$. It should be noted that, in this case, the pulse train of the Stokes radiation shifted to the rear of the pulse train of the pump laser radiation with a decrease in the SRS oscillation efficiency. A similar temporal pattern (as in Figure 6b) of the degraded generation of both Stokes and anti-Stokes radiation was also observed at $|\Delta L| > 5$ mm even in the case of $\varphi \leq 27^\circ$.

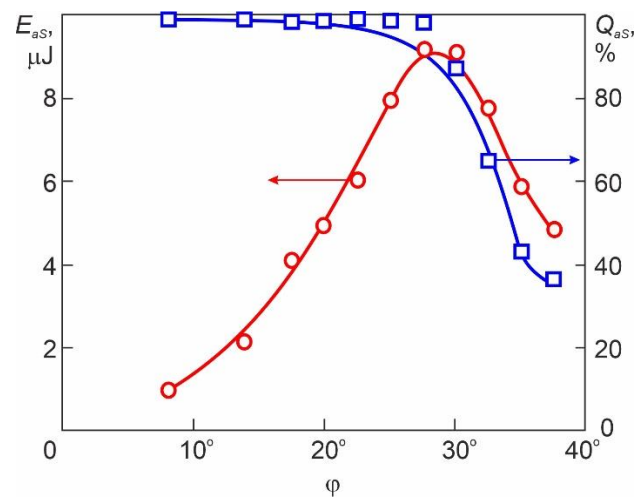


Figure 6. Dependence of the anti-Stokes pulse train energy E_{aS} and the single anti-Stokes pulse self-separation quality Q_{aS} on the rotation angle φ of the active CaMoO_4 element. Points are the experimental results. Lines are the modeling results.

Figure 6 shows the dependence of the anti-Stokes pulse train energy E_{aS} and the single anti-Stokes pulse self-separation quality Q_{aS} (equal to energy of the most intense anti-Stokes pulse divided by the total energy of the anti-Stokes pulse train) on the rotation angle φ of the active CaMoO_4 element, measured using the energy meter StarLite (Ophir-Spiricon).

It can be seen from Figure 6 that the anti-Stokes pulse train energy had a maximum of $E_{max} = 9 \mu\text{J}$ at $\varphi_{opt} = 27^\circ\text{--}30^\circ$. It can also be seen that, at $\varphi < 30^\circ$, a high-quality self-separation of a single ultrashort pulse of the anti-Stokes radiation with $Q_{aS} > 90\%$ was achieved. At $\varphi > 30^\circ$, the Q_{aS} value decreased sharply because the train of several (two and three) anti-Stokes pulses was generated, but the anti-Stokes pulse train energy decreased.

The decrease in the anti-Stokes radiation energy at $\varphi < \varphi_{opt}$ is explained by a decrease in the fraction ($\sin\varphi$) of an ordinary wave in the pump laser radiation, which is scattered into an anti-Stokes ordinary wave in the parametric Raman process [15].

The decrease in the anti-Stokes radiation energy at $\varphi > \varphi_{opt}$ can be explained by a decrease in the pump laser oscillation efficiency when introducing losses ($\cos\varphi$) in the pump laser having a polarizer P inside the cavity (Figure 3), and, as a consequence, a decrease in the efficiency of SRS conversion into the Stokes radiation. This is confirmed by the measurements of the dependences of the pulse train energy of the pump laser and Stokes radiations on the φ angle. The pulse train energy of the pump laser radiation monotonically decreased from $237 \mu\text{J}$ at $\varphi = 0$ down to $161 \mu\text{J}$ at $\varphi = 40^\circ$. At the same time, the pulse train energy of the Stokes radiation also monotonously decreased from $219 \mu\text{J}$ to $83 \mu\text{J}$.

An individual pulse duration of the output radiation was also measured using a PS-1/S1 picosecond streak camera [29] (GPI RAS). The pulse duration of the pump laser radiation was $\tau_p = 17$ ps with a distorted pulse shape indicating depletion in the process of nonlinear conversion. For the Stokes and anti-Stokes radiation, a shortened pulse duration of $\tau_{osc} = 9$ ps was recorded with a Gaussian pulse shape that is close to the estimation

of pulse shortening in synchronously pumped lasers $\tau_{osc} \approx (\tau_p \cdot \tau_R)^{0.5} \approx 6$ ps [30], where $\tau_R = 1/(\pi \cdot c \cdot \Delta\nu_R) = 2$ ps is the phase relaxation time and c is the velocity of light in vacuum.

The light polarization analysis for the output laser radiation showed that the Stokes radiation was polarized in the phase-matching plane of the CaMoO₄ crystal (an extraordinary wave), which is explained by a higher Raman gain coefficient for the extraordinary wave ($g_e > g_o$). The anti-Stokes radiation was polarized perpendicular to the phase-matching plane of the CaMoO₄ crystal (an ordinary wave), which confirms the fulfillment of the phase matching of the *ooee* type.

5. Mathematical Modeling

A system of rate equations describing the pump laser oscillation ($\lambda_p = 1064$ nm) can be written as follows:

$$\begin{aligned} \pm \frac{\partial I^{(\pm)}}{\partial z} + \frac{n_a}{c} \frac{\partial I^{(\pm)}}{\partial t} &= \alpha \left(I^{(\pm)} + I_0 \right) - k_a I^{(\pm)}, \\ \frac{\partial \alpha}{\partial t} &= - \frac{\alpha}{\hbar \omega_p / \sigma_{em}} \left(I^{(+)} + I^{(-)} \right) + \frac{\alpha_0 - \alpha}{\tau}, \end{aligned} \quad (3)$$

where $I^{(\pm)}$ is the intensity of the pumped laser radiation, propagating forward (+) and backward (−) in the active Nd:YAG element; I_0 is the intensity of seed radiation at $\lambda_p = 1064$ nm; α is the gain coefficient of the active Nd:YAG element; α_0 is the pump parameter; $\hbar \omega_p$, σ_{em} , τ , and n_a are the photon energy, the effective emission cross-section, the upper laser level lifetime, and the refractive index of the active Nd:YAG element, respectively ($\hbar \omega_p = 1.87 \cdot 10^{-19}$ J, $\sigma_{em} = 2.8 \cdot 10^{-19}$ cm², $\tau = 230$ μ s, and $n_a = 1.82$ [31]); k_a is the loss coefficient of the active Nd:YAG element; z is the longitudinal coordinate; t is time; and c is the velocity of light in vacuum.

A system of rate equations describing the four-wave interaction in the active CaMoO₄ element of the parametric Raman laser can be written as follows:

$$\begin{aligned} \pm \frac{\partial A_o^{(\pm)}}{\partial z} + \frac{n_b}{c} \frac{\partial A_o^{(\pm)}}{\partial t} &= - \frac{g_o}{2} \frac{\lambda_p}{\lambda_{aS}} \left(|P_o^{(+)}|^2 + |P_o^{(-)}|^2 \right) A_o^{(\pm)} - \frac{p}{2} \frac{\lambda_p}{\lambda_{aS}} P_o^{(\pm)} P_e^{(\pm)} S_e^{(\pm)*} - \frac{k_b}{2} A_o^{(\pm)}, \\ \pm \frac{\partial P_o^{(\pm)}}{\partial z} + \frac{n_b}{c} \frac{\partial P_o^{(\pm)}}{\partial t} &= \frac{g_o}{2} \left(|A_o^{(+)}|^2 + |A_o^{(-)}|^2 \right) P_o^{(\pm)} - \frac{g_o}{2} \frac{\lambda_S}{\lambda_p} \left(|S_o^{(+)}|^2 + |S_o^{(-)}|^2 \right) P_o^{(\pm)} - \frac{k_b}{2} P_o^{(\pm)}, \\ \pm \frac{\partial P_e^{(\pm)}}{\partial z} + \frac{n_b}{c} \frac{\partial P_e^{(\pm)}}{\partial t} &= - \frac{g_e}{2} \frac{\lambda_S}{\lambda_p} \left(|S_e^{(+)}|^2 + |S_e^{(-)}|^2 \right) P_e^{(\pm)} - \frac{k_b}{2} P_e^{(\pm)}, \\ \pm \frac{\partial S_e^{(\pm)}}{\partial z} + \frac{n_b}{c} \frac{\partial S_e^{(\pm)}}{\partial t} &= \frac{g_e}{2} \left(|P_e^{(+)}|^2 + |P_e^{(-)}|^2 \right) \left(S_e^{(\pm)} + \sqrt{I_{S0}} \right) + \frac{p}{2} P_e^{(\pm)} P_o^{(\pm)} A_o^{(\pm)*} - \frac{k_b}{2} S_e^{(\pm)}, \end{aligned} \quad (4)$$

where g_o and g_e are the Raman gain coefficients for the ordinary and extraordinary waves, respectively; p is the parametric coefficient determined by Equation (2); $A_o^{(\pm)}$ is the ordinary wave amplitude of the anti-Stokes radiation ($\lambda_{aS} = 973$ nm) generated by parametric Raman four-wave mixing at the *ooee*-type phase matching [16]; $P_e^{(\pm)}$ is the extraordinary wave amplitude of the pump laser radiation ($\lambda_p = 1064$ nm) being the pump wave for the four-wave-mixing process; $P_o^{(\pm)}$ is the ordinary wave amplitude of the pump laser radiation ($\lambda_p = 1064$ nm) being the probe wave scattering into the anti-Stokes wave in the four-wave mixing process; $S_e^{(\pm)}$ is the extraordinary wave amplitude of the Stokes radiation ($\lambda_S = 1174$ nm) generated by SRS; n_b and k_b are the refractive index and the loss coefficient of the active CaMoO₄ element, respectively; and $I_{S0} \approx 10^{-13} (|P_e^{(+)}|^2 + |P_e^{(-)}|^2)$ is the intensity of seed Stokes radiation at $\lambda_S = 1174$ nm. The second term in the right part of the first and last equations describe the parametric interaction under the phase-matching conditions ($\Delta k = 0$). In equations system (4), we neglected to describe the SRS generation of the Stokes radiation ordinary wave (that does not participate in the *ooee*-type four-wave-mixing process) because of the significantly lower relative efficiency of its generation compared to the Stokes extraordinary wave due to $g_o < g_e$ and $|P_o^{(\pm)}|^2 < |P_e^{(\pm)}|^2$.

The boundary conditions corresponding to the optical scheme (Figure 3) can be written as follows:

$$\begin{aligned}
 I^{(+)}(t, z = 0) &= I^{(-)}(t, z = 0) \cdot T_Q^2 \cdot T_{fa}^2, \\
 I^{(-)}(t, z = L_a) &= \left(\left| P_e^{(-)}(t - t_{free}, z = 0) \right|^2 + \left| P_o^{(-)}(t - t_{free}, z = 0) \right|^2 \right) \cdot T_{fa} \cdot T_{fb} / (r_a / r_b)^2, \\
 P_e^{(+)}(t, z = 0) &= \sqrt{I^{(+)}(t - t_{free}, z = L_a)} \cdot \cos \varphi \cdot \sqrt{T_{fa} \cdot T_{fb} \cdot (r_a / r_b)^2}, \\
 P_e^{(-)}(t, z = L_b) &= P_e^{(+)}(t, z = L_b) \cdot \sqrt{T_{fb}^2 \cdot R_p}, \\
 P_o^{(+)}(t, z = 0) &= \sqrt{I^{(+)}(t - t_{free}, z = L_a)} \cdot \sin \varphi \cdot \sqrt{T_{fa} \cdot T_{fb} \cdot (r_a / r_b)^2}, \\
 P_o^{(-)}(t, z = L_b) &= P_o^{(+)}(t, z = L_b) \cdot \sqrt{T_{fb}^2 \cdot R_p}, \\
 S_e^{(+)}(t, z = 0) &= S_e^{(-)}(t - 2t_{free} - 2t_a - 2\Delta L / c, z = 0) \cdot \sqrt{T_{fb}^2 \cdot R_{S2}}, \\
 S_e^{(-)}(t, z = L_b) &= S_e^{(+)}(t, z = L_b) \cdot \sqrt{T_{fb}^2 \cdot R_S}, \\
 A_o^{(+)}(t, z = 0) &= A_o^{(-)}(t - 2t_{free} - 2t_a - 2\Delta L / c, z = 0) \cdot \sqrt{T_{fb}^2 \cdot R_{aS2}}, \\
 A_o^{(-)}(t, z = L_b) &= 0,
 \end{aligned} \tag{5}$$

where T_Q is the transmission coefficient of the passive laser shutter; L_a and L_b are the lengths of the active Nd:YAG and CaMoO₄ elements, respectively; T_{fa} and T_{fb} are the transmission coefficients of the faces of the active Nd:YAG and CaMoO₄ elements, respectively; r_a / r_b is the ratio of the beam radius in the active Nd:YAG element to the beam radius in the active CaMoO₄ element, regulated by the optical system; R_p and R_S are the reflection coefficients of the output coupler (OC) at the wavelengths of $\lambda_p = 1064$ nm and $\lambda_S = 1174$ nm, respectively ($R_{aS} = 0$ at $\lambda_{aS} = 973$ nm); R_{S2} and R_{aS2} are the reflection coefficients of the end mirror (M2) of the parametric Raman laser cavity at the wavelengths of $\lambda_S = 1174$ nm and $\lambda_{aS} = 973$ nm, respectively; $t_{free} = L_{free} / c$ is the transit time of the free space between the active Nd:YAG and CaMoO₄ elements; L_{free} is the distance between the active Nd:YAG and CaMoO₄ elements; t_a is the transit time of the active Nd:YAG element; ΔL is the difference in optical lengths of cavities of the parametric Raman laser and the pump laser; and φ is the rotation angle of the active CaMoO₄ element. It is also assumed that the pumping mirror (PM) of the parametric Raman laser is highly transmissive for the pump laser radiation and highly reflective for the radiation oscillating in the parametric Raman laser.

Oscillation in the pump laser that has the passive laser shutter begins at the moment when the gain α increases (under the action of optical pumping) to the threshold value α_{th} equal to the loss coefficient of the pump laser cavity at the initial state of the shutter:

$$\alpha_{th} = - \frac{\ln(T_{Q0}^2 T_a^2 T_b^2 R_p)}{2L_a}, \tag{6}$$

where T_{Q0} is an initial transmittance of the shutter (the closed state of the shutter); $T_a = T_{fa}^2 \exp(-k_a L_a)$ is the transmission coefficient of the active Nd:YAG element; and $T_b = T_{fb}^2 \exp(-k_b L_b)$ is the transmission coefficient of the active CaMoO₄ element. Then, there is a linear stage of lasing, at the end of which the shutter absorption is saturated to the maximum transmission value T_{Q1} (the open state of the shutter). In boundary conditions (5), we used $T_Q = T_{Q1}$. At the same time, we used the approximation of instantaneous shutter opening at the moment when the α_{th} threshold value of the gain is reached. We took the instantaneous opening of the shutter as the starting point of the calculation. Then, the initial calculation conditions were as follows. The initial values of the intensities and amplitudes of all interacting waves were equal to zero, and the initial value of the gain was assumed to be equal to α_{th} . We also believe that the duration of the oscillating giant pulse of the pump laser radiation in the passive Q-switching regime should be significantly

shorter than the upper laser level lifetime (τ) of the active Nd:YAG element; therefore, we neglected the last term in the second equation of the equations system (3).

Figure 7 demonstrates the simulation result of the laser oscillation at $R_p = R_S = 95\%$, $R_{S2} = 100\%$, $R_{aS2} = 0\%$, $L_a = 10$ cm, $L_b = 3$ cm, $k_a = k_b = 0.01$ cm⁻¹, $T_{fa} = T_{fb} = 99.5\%$, $L_{free} = 107$ cm, $\Delta L = 0$, $T_{Q0} = 40\%$, $T_{Q1} = 85\%$, $\varphi = 27^\circ$, and $r_a/r_b = 2.2$. The angle φ was chosen at an optimal value (27°), providing the highest intensity of anti-Stokes generation. It can be seen that, in the Q-switching regime, the output giant pulse of the pump laser radiation (green line) has a modulation with a period equal to a round-trip time of the pump laser cavity $t_{cav} = L_{cav} / c = 8.7$ ns ($L_{cav} = L_{free} + L_a \cdot n_a + L_b \cdot n_b = 131$ cm is the optical length of the pump laser cavity). In this case, the output Stokes (red line) and anti-Stokes (blue line) radiation of the parametric Raman laser oscillates in the form of trains of ultrashort radiation pulses with a repetition period equal to t_{cav} . It should be noted that the r_a/r_b ratio was increased up to a value of 2.2 to increase the SRS conversion efficiency, which provides the shortening of the anti-Stokes pulse train to a duration close to t_{cav} for the self-separation of only one intense anti-Stokes pulse in the anti-Stokes pulse train. However, the quality of this self-separation is not very high.

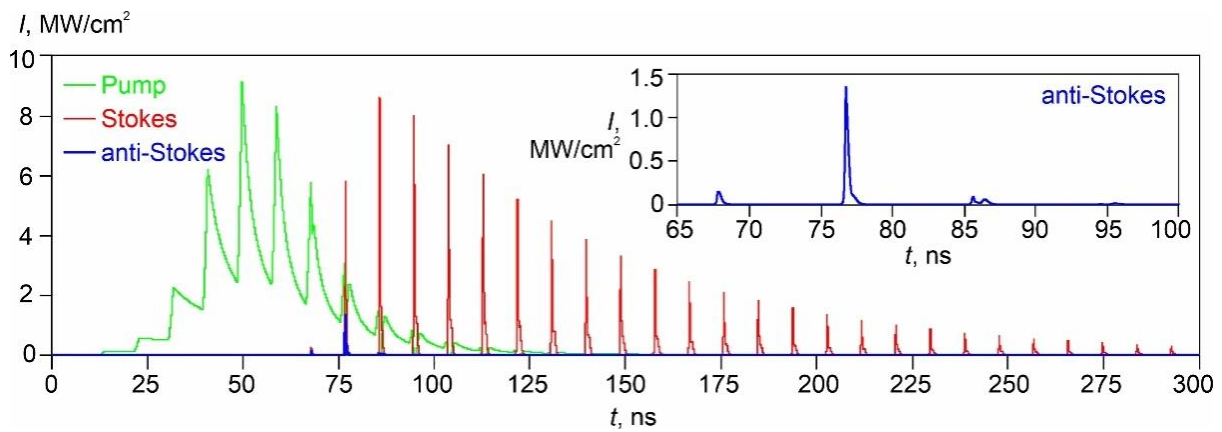


Figure 7. The simulation result of the passively Q-switched laser oscillation for the shutter with $T_{Q0} = 40\%$ and $T_{Q1} = 85\%$ at $\varphi_{opt} = 27^\circ$.

A similar temporal pattern of oscillation was previously observed in an experimental study on the oscillation of the zero-dispersion phase-matched parametric Raman CaCO₃ laser under intracavity pumping by a passively Q-switched 1338 nm Nd:YAG laser [7].

The high-quality self-separation of a single ultrashort anti-Stokes pulse can be organized using a high-speed repetitively pulsed laser shutter with a modulation period equal to t_{cav} , which usually provides a mode-locking regime of laser oscillation. The modulation can be passive (when using a rapidly relaxing saturable absorber as a passive laser shutter) or active (when using a rapidly acting active laser shutter synchronized with t_{cav}). For the simplicity of modeling, we chose the second option. Then, in boundary conditions (5), the transmission coefficient of the laser shutter T_Q should be modulated in time as follows:

$$T_Q(t) = T_{Q0} + (T_{Q1} - T_{Q0}) \cdot \sum_{i=1}^N \exp \left[- \left(\frac{t - N \cdot t_{res} + t_{res}}{t_{open}/2} \right)^2 \right], \quad (7)$$

where N is the number of Gaussian pulses of the shutter opening ($N \cdot t_{cav}$ is equal to the calculation time) and t_{open} is the duration of the pulse of the opening state of the shutter.

Figure 8 demonstrates the simulation results for $T_Q(t)$ determined by Equation (7) with $t_{open} = 2$ ns at three values of the φ rotation angle using the same values of other input parameters, except for the r_a/r_b ratio, which was reduced to $r_a/r_b = 1.5$ as in the experiment.

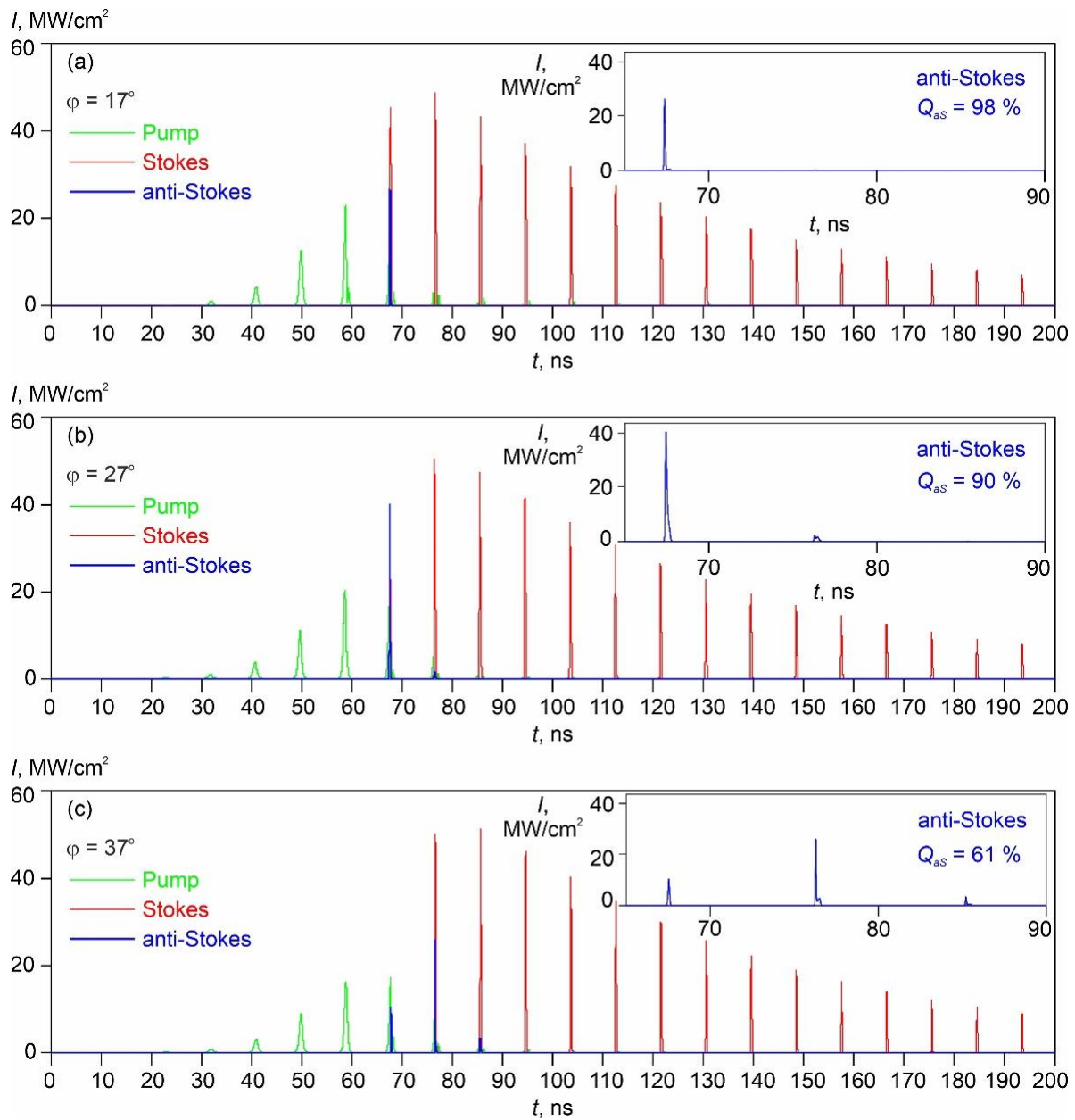


Figure 8. The simulation results of the mode-locked laser oscillation for the shutter with $t_{open} = 2$ ns at (a) $\varphi = 17^\circ$, (b) $\varphi = 27^\circ$, and (c) $\varphi = 37^\circ$.

It can be seen from Figure 8 that the use of the rapidly acting shutter led to the generation of an intense ultrashort pulse train of the pump laser radiation (green line), which is similar in result to the mode-locking regime. Despite the small value of r_a/r_b , we can also see the efficient SRS oscillation of a train of ultrashort Stokes pulses (red line), which ensures the generation of a single intense ultrashort anti-Stokes pulse (blue line). The radiation pulses turned out to be significantly shorter and more intense than in the previous case. However, it should be noted that we used a single-mode model, so the duration of ultrashort pulses here depends on the inertia of the shutter (the t_{open} duration), but when the laser cavity modes are locked, the pulse duration should be determined by the number of locked modes. Consequently, our single-mode model does not provide correct information about the duration of the ultrashort radiation pulses, but adequately describes the mechanism for the self-separation of a single intense ultrashort anti-Stokes pulse by energy density. Thus, at $\varphi = 17^\circ$ (Figure 8a), a part of energy density in the output anti-Stokes radiation is low and amounts to $E_{aS} = 0.4\%$ of the active Nd:YAG

element-stored energy density ($=\alpha_{th} L_a \hbar\omega_p / \sigma_{em}$), but the self-separation quality of a single anti-Stokes pulse is very high ($Q_{aS} = 98\%$). At the optimum value of $\varphi = 27^\circ$ (Figure 8b), the energy density part in the anti-Stokes radiation reaches its maximum value and amounts to $E_{aS} = 1\%$ of the active Nd:YAG element-stored energy density. The self-separation quality is still high ($Q_{aS} = 90\%$). At the higher angle of $\varphi = 37^\circ$ (Figure 8c), the anti-Stokes energy density part and self-separation quality decrease to $E_{aS} = 0.5\%$ and $Q_{aS} = 61\%$, respectively. The fully calculated dependences of E_{aS} and Q_{aS} on φ are shown by lines in Figure 6, where we can see a good agreement with the experimental points.

6. Conclusions

The conditions for the self-separation of a single ultrashort pulse at an anti-Stokes wavelength of 973 nm with a pulse duration of 9 ps and pulse energy of up to 9 μ J in a parametric Raman anti-Stokes CaMoO₄ laser with collinear phase-matching insensitive to angular mismatch under intracavity synchronous pumping by a mode-locked 1064 nm Nd:YAG laser were experimentally investigated and theoretically simulated. When the rotation angle of the active CaMoO₄ element was optimum ($\varphi_{opt} = 27^\circ$ – 30°) and the initial transmission of the passive laser shutter was low enough (40 %) for the chosen ratio of the beam radii in the active Nd:YAG and CaMoO₄ elements ($r_a/r_b = 1.5$), the separated anti-Stokes pulse energy was maximal (9 μ J) with a high self-separation quality (90%). In conclusion, it should be noted that the initial transmission of the shutter can be increased, but to compensate for this, the r_a/r_b ratio must also be increased to ensure a highly efficient SRS with the high-quality self-separation of a single anti-Stokes pulse. This opens up the possibility of using passive solid-state shutters with a long service life.

Author Contributions: Conceptualization, S.N.S.; methodology, A.G.P. and S.N.S.; software, E.V.S. and Y.A.K.; validation, S.N.S.; formal analysis, M.D.L. and D.P.T.; investigation, D.P.T., A.G.P., E.V.S. and S.N.S.; resources, K.A.S., D.A.L., V.E.S. and A.I.T.; data curation, Y.A.K., V.E.S. and D.P.T.; writing—original draft preparation, S.N.S. and D.P.T.; writing—review and editing, S.N.S. and A.G.P.; visualization, D.P.T.; supervision, S.N.S. All authors have read and agreed to the published version of the manuscript.

Funding: This research was funded by Russian Science Foundation—Project No 22-22-00708 (<https://rscf.ru/project/22-22-00708/>, accessed on 3 April 2023).

Institutional Review Board Statement: Not applicable.

Informed Consent Statement: Not applicable.

Data Availability Statement: Not applicable.

Conflicts of Interest: The authors declare no conflict of interest.

References

1. Grasyuk, A.Z.; Losev, L.L.; Lutsenko, A.P.; Sazonov, S.N. Parametric Raman anti-Stokes laser. *Sov. J. Quantum Electron.* **1990**, *20*, 1153–1155. [[CrossRef](#)]
2. Mildren, R.P.; Coutts, D.W.; Spence, D.J. All-solid-state parametric Raman anti-Stokes laser at 508 nm. *Opt. Express* **2009**, *17*, 810–818. [[CrossRef](#)] [[PubMed](#)]
3. Wang, A.; Cong, Z.; Qin, Z.; Zhang, X.; Wei, W.; Wang, W.; Zhang, Y.; Zhang, H.; Yu, H. LD-side-pumped Nd:YAG/BaWO₄ intracavity Raman laser for anti-Stokes generation. *Opt. Commun.* **2014**, *322*, 44–47. [[CrossRef](#)]
4. Pan, J.; Shen, Y.; Wan, Z.; Fu, X.; Zhang, H.; Liu, Q. Index-tunable structured-light beams from a laser with an intracavity astigmatic mode converter. *Phys. Rev. Appl.* **2020**, *14*, 044048. [[CrossRef](#)]
5. Jia, W.; Gao, C.; Zhao, Y.; Li, L.; Wen, S.; Wang, S.; Bao, C.; Jiang, C.; Yang, C.; Yang, Y. Intracavity spatiotemporal metasurfaces. *Adv. Photonics* **2023**, *5*, 026002. [[CrossRef](#)]
6. Smetanin, S.N.; Jelínek, M.; Kubeček, V.; Jelínková, H.; Ivleva, L.I. Parametric second Stokes Raman laser output pulse shortening to 300 ps due to depletion of pumping of intracavity Raman conversion. *Appl. Phys. B* **2016**, *122*, 260. [[CrossRef](#)]
7. Smetanin, S.N.; Jelínek, M.; Tereshchenko, D.P.; Ershkov, M.N.; Kubeček, V. Laser pulse shortening via zero-dispersion phase matching of parametric Raman interactions in crystals. *Crystals* **2021**, *11*, 19. [[CrossRef](#)]
8. Cheng, T.; Chen, X.; Yan, X.; Zhang, X.; Wang, F.; Suzuki, T.; Ohishi, Y. Mid-infrared stimulated Raman scattering and four-wave mixing in a tellurite microstructured optical fiber. *IEEE Photonics Technol. Lett.* **2022**, *34*, 239. [[CrossRef](#)]

9. Smetanin, S.N.; Jelínek, M.; Kubeček, V. Parametric Raman crystalline anti-Stokes laser at 503 nm with collinear beam interaction at tangential phase matching. *Appl. Phys. B* **2017**, *123*, 203. [[CrossRef](#)]
10. Nikogosyan, D.N. *Nonlinear Optical Crystals: A Complete Survey*; Springer: New York, NY, USA, 2005.
11. Giordmaine, J.A.; Kaiser, W. Light scattering by coherently driven lattice vibrations. *Phys. Rev.* **1966**, *144*, 676–688. [[CrossRef](#)]
12. Alfano, R.R.; Shapiro, S.L. Optical phonon lifetime measured directly with picosecond pulses. *Phys. Rev. Lett.* **1971**, *26*, 1247–1251. [[CrossRef](#)]
13. Akhmanov, S.A.; Dmitriev, V.G.; Kovrigin, A.I.; Koroteev, N.I.; Tunkin, V.G.; Kholodykh, A.I. Active spectroscopy of Raman scattering of light with the aid of a quasicontinuously tunable parametric generator. *JETP Lett.* **1972**, *15*, 425–428.
14. Akhmanov, S.A.; Koroteev, N.I. Spectroscopy of light scattering and nonlinear optics. Nonlinear-optical methods of active spectroscopy of Raman and Rayleigh scattering. *Sov. Phys. Uspekhi* **1977**, *20*, 899–936. [[CrossRef](#)]
15. Smetanin, S.N.; Jelínek, M.; Tereshchenko, D.P.; Kubeček, V. Extracavity pumped parametric Raman nanosecond crystalline anti-Stokes laser at 954 nm with collinear orthogonally polarized beam interaction at tangential phase matching. *Opt. Express* **2018**, *26*, 22637–22649. [[CrossRef](#)]
16. Smetanin, S.N.; Jelínek, M.; Tereshchenko, D.P.; Shukshin, V.E.; Konyukhov, M.V.; Papashvili, A.G.; Voronina, I.S.; Ivleva, L.I.; Kubeček, V. Nanosecond parametric Raman anti-Stokes SrWO₄ laser at 507 nm with collinear phase matching. *Opt. Express* **2020**, *28*, 22919–22932. [[CrossRef](#)]
17. Basiev, T.T.; Sobol, A.A.; Voronko, Y.K.; Zverev, P.G. Spontaneous Raman spectroscopy of tungstate and molybdate crystals for Raman lasers. *Opt. Mater.* **2000**, *15*, 205–216. [[CrossRef](#)]
18. Basiev, T.T.; Doroshenko, M.E.; Ivleva, L.I.; Osiko, V.V.; Kosmyna, M.B.; Komar, V.K.; Sulc, J.; Jelinkova, H. Lasing properties of selectively pumped Raman-active Nd³⁺-doped molybdate and tungstate crystals. *Quantum Electron.* **2006**, *36*, 720–726. [[CrossRef](#)]
19. Yu, H.; Li, Z.; Lee, A.J.; Li, J.; Zhang, H.; Wang, J.; Pask, H.M.; Piper, J.A.; Jiang, M. A continuous wave SrMoO₄ Raman laser. *Opt. Lett.* **2011**, *36*, 579–581. [[CrossRef](#)] [[PubMed](#)]
20. Frank, M.; Smetanin, S.N.; Jelínek, M.; Vyhliđal, D.; Shukshin, V.E.; Ivleva, L.I.; Dunaeva, E.E.; Voronina, I.S.; Zverev, P.G.; Kubeček, V. Stimulated Raman scattering in alkali-earth tungstate and molybdate crystals at both stretching and bending Raman modes under synchronous picosecond pumping with multiple pulse shortening down to 1 ps. *Crystals* **2019**, *9*, 167. [[CrossRef](#)]
21. Kaminskii, A.A.; Bagaev, S.N.; Ueda, K.; Takaichi, K.; Eichler, H.J. High-order picosecond SRS and self-SRS generation in Nd³⁺-doped CaMoO₄, SrMoO₄, and SrWO₄ laser crystals. *Crystallogr. Rep.* **2002**, *47*, 653–657. [[CrossRef](#)]
22. Basiev, T.T.; Zverev, P.G.; Karasik, A.Y.; Osiko, V.V.; Sobol, A.A.; Chunaev, D.S. Picosecond stimulated Raman scattering in crystals. *JETP* **2004**, *99*, 934–941. [[CrossRef](#)]
23. Blistanov, A.A.; Galagan, B.I.; Denker, B.I.; Ivleva, L.I.; Osiko, V.V.; Polozkov, N.M.; Sverchkov, Y.E. Spectral and lasing characteristics of CaMoO₄:Nd³⁺ single crystals. *Sov. J. Quantum Electron.* **1989**, *19*, 747–748. [[CrossRef](#)]
24. Smetanin, S.N.; Jelínek, M.; Kubeček, V.; Jelínková, H.; Ivleva, L.I.; Shurygin, A.S. Four-wave-mixing and nonlinear cavity dumping of 280 picosecond 2nd Stokes pulse at 1.3 μm from Nd:SrMoO₄ self-Raman laser. *Laser Phys. Lett.* **2016**, *13*, 015801. [[CrossRef](#)]
25. Smetanin, S.N.; Fedin, A.V.; Shurygin, A.S. Realisation of four-wave mixing phase matching for frequency components at intracavity stimulated Raman scattering in a calcite crystal. *Quantum Electron.* **2013**, *43*, 512–518. [[CrossRef](#)]
26. Bass, M. *Handbook of Optics: Volume IV—Optical Properties of Materials, Nonlinear Optics, Quantum Optics*, 3rd ed.; The McGraw-Hill Companies, Inc.: New York, NY, USA, 2010.
27. Loudon, R. The Raman effect in crystals. *Adv. Phys.* **1964**, *13*, 423–482. [[CrossRef](#)]
28. Bezrodnyi, V.I.; Ponezha, E.A.; Tikhonov, E.A. A new passive Q switch for Nd³⁺ lasers. *Sov. J. Quantum Electron.* **1978**, *8*, 34–37. [[CrossRef](#)]
29. Vorobiev, N.S.; Gornostaev, P.B.; Lozovoi, V.I.; Smirnov, A.V.; Shashkov, E.V.; Schelev, M.Y. A PS-1/S1 picosecond streak camera in experimental physics. *Instrum. Exp. Tech.* **2016**, *59*, 551–556. [[CrossRef](#)]
30. Nekhaenko, V.A.; Pershin, S.M.; Podshivalov, A.A. Synchronously pumped tunable picosecond lasers (review). *Sov. J. Quantum Electron.* **1986**, *16*, 299–316. [[CrossRef](#)]
31. Svelto, O. *Principles of Lasers*, 5th ed.; Springer: New York, NY, USA, 2010.

Disclaimer/Publisher’s Note: The statements, opinions and data contained in all publications are solely those of the individual author(s) and contributor(s) and not of MDPI and/or the editor(s). MDPI and/or the editor(s) disclaim responsibility for any injury to people or property resulting from any ideas, methods, instructions or products referred to in the content.